



# Effect of the Heat Input on Wire-Arc Additive Manufacturing of Invar 36 Alloy: Microstructure and Mechanical Properties

Fernando Veiga<sup>1,2</sup> · Alfredo Suárez<sup>1,3</sup> · Teresa Artaza<sup>1</sup> · Eider Aldalur<sup>1</sup>

Received: 25 October 2021 / Accepted: 28 March 2022 / Published online: 7 April 2022  
© The Author(s) 2022

## Abstract

Invar, also known as FeNi36, is a material of great interest due to its unique properties, which makes it an excellent alternative for sectors such as tooling in aeronautics and aerospace. Its manufacture by means of wire arc additive manufacturing (WAAM) technology could extend its use. This paper aims to evaluate the comparison of two of the most widespread WAAM technologies: plasma arc welding (PAW) and gas metal arc welding (GMAW). This comparison is based on the analysis of wall geometry, metallography, and mechanical properties of the material produced by both technologies. The results show a slight increase in toughness and elongation before fracture and worse tensile strength data in the case of PAW, with average values of 485 MPa for ultimate tensile strength (UTS), 31% for elongation and 475 MPa, 40% in GMAW and PAW, respectively. All results gathered from the analysis show the possibility of successful manufacturing of Invar by means of WAAM technologies. The novelties presented in this paper allow us to establish relationships between the thermal input of the process itself and the mechanical and metallographic properties of the material produced.

**Keywords** Nickel-based alloys · Direct energy deposition · WAAM · Additive manufacturing · FeNi36

## 1 Introduction

Throughout history, humanity has been in search of new materials that can improve the quality and would enable a better fabrication of daily used items. Nowadays, the advance

in new technologies and manufacturing processes has led to creating new materials with applications that would have never been possible in the past. One of these materials is Invar 36, also known as FeNi36 (designed as K93600 by the unified numbering system UNS). It is a Fe-based alloy, composed of nickel and iron forming a solid solution that commercially has a composition of about 64 wt% Fe–36 wt% Ni [1]. The main quality of this type of alloy is the low CTE (coefficient of thermal expansion) value that it has.

The most common way of manufacturing Invar 36 alloy is machining. However, the machinability of this type of material is poor and it presents some problems. The high ductility (between 0.06 and 0.45), the low heat conductivity (between 12 and 15 W/m K) and the considerable work hardening that presents this material are the main reasons for these problems. Specifically, in machining processes of Invar alloy, ductile chips are formed in the cutting faces, which results in much greater tool wear. This means having processes with very poor efficiency, which leads to a high cost [2]. Due to this poor machining, new ways of manufacturing Invar alloy parts are necessary.

Additive manufacturing (AM) is one of the alternatives to machining the Invar alloys. AM brings a solution to the problems presented above and uses the minimum amount of material achieving high material usage efficiency.

---

Recommended for publication by Commission I—Additive Manufacturing, Surfacing, and Thermal Cutting.

✉ Fernando Veiga  
fernando.veiga@tecnalia.com; fernando.veiga@unavarra.es

✉ Teresa Artaza  
teresa.artaza@tecnalia.com

Alfredo Suárez  
alfredo.suarez@tecnalia.com

Eider Aldalur  
eider.aldalur@tecnalia.com

<sup>1</sup> TECNALIA, Basque Research and Technology Alliance (BRTA), Parque Científico Y Tecnológico de Gipuzkoa, Paseo Mikeletegi 7, 20009 Donostia-San Sebastián, Spain

<sup>2</sup> Departamento de Ingeniería, Universidad Pública de Navarra, Edificio Departamental Los Pinos, Campus Arrosadía, 31006 Pamplona, Navarra, Spain

<sup>3</sup> ADDILAN Fabricación Aditiva S.L., Eguzkitza 1, 48200 Durango, Spain

Furthermore, the design freedom that can be achieved with this type of process is very high. In previous literature, different additive manufacturing technologies were used to manufacture Invar parts [3], mostly, laser-based powder bed fusion of metals (PBF-LB/M) and power/laser directed energy deposition.

Yakout et al. [4] manufactured Invar samples with different parameters and consecutively, different energy densities utilizing PBF-LB/M technology. Optimum process parameters and specifically, optimum laser energy density ranges were suggested after analyzing the density, the mechanical properties, the composition and the microstructure of the samples. For Invar 36, with laser energy density below the brittle-ductile transition energy density ( $52.1 \text{ J/mm}^3$ ), the void formation is elevated and a brittle fracture is observed. Between the brittle-ductile transition energy density and the critical energy density ( $86.8 \text{ J/mm}^3$ ), parts have the highest density, high toughness, and medium tensile strength. Up to this last energy, the chemical composition of the material is changed and the mechanical properties are reduced. Wei et al. [5] also analyzed the mechanical properties of the PBF-LB/M manufactured Invar samples. In this study, was concluded that the optimal laser energy density was  $99.2 \text{ J/mm}^3$  obtaining approximately full density, the ultimate tensile strength of 480 MPa and Vickers hardness of 1.8 GPa.

Moreover, regarding the microstructure of Invar manufactured utilizing PBF-LB/M, Yang et al. [6] and Qiu et al. [7] confirmed that is composed of columnar  $\gamma$  grains with an FCC structure and nanosized BCC  $\alpha$  precipitates, which is in accordance with the microstructure obtained in wrought Invar.

Also, power/laser directed energy deposition technology was utilized to manufacture Invar parts. For example, Liu et al. [8] studied experimentally and via simulations the heat accumulation in this type of processes. Furthermore, Zhan et al. [9] studied the effect of the heat input on the microstructure and the orientation of the grains, employing optical microscopy, finding that the orientation of the cellular crystals is highly influenced by the heat flow, and consequently by the scanning direction. Finally, Li et al. [10] analyzed the microstructure evolution and the mechanical properties of Invar samples manufactured utilizing power/laser directed energy deposition. Going a step further, different authors have also manufactured functionally graded material from Ti-6Al-4 V to Invar using power/laser directed energy deposition technology and depth analysis of the interface was performed [11, 12].

Traditionally, powder has been the most widely used raw material for AM. However, in recent years, more attention has been paid to processes that utilize wire material and an electric arc. These processes are able to solve several problems that the powder feed processes cause. Specifically, some of these issues are the low deposition rate, the high cost, aspects related to safety and material reuse [13, 14].

In this way, there are few studies about the utilization of wire arc additive manufacturing (WAAM) process to manufacture Invar parts [15]. Most are focused on the use of the WAAM to manufacture aeronautical tools to reduce costs and the amount of raw material [16]. For this application, the Invar material is of vital importance due to its already named small CTE value. Depending on the nature of the energy source, three types of WAAM processes are distinguished: gas metal arc welding (GMAW), gas tungsten arc welding (GTAW), and plasma arc welding (PAW)-based WAAM processes. In previous literature, only GMAW-based WAAM process was studied for Invar manufacturing [17]. Finally, in some studies, Invar alloy is combined with structural steel thanks to the WAAM process to adapted locally the mechanical properties of the deposited material [18, 19].

## 2 Materials and Methods

### 2.1 Setup, Deposition Strategy

An ADDILAN WAAM 3 axis machine equipped with a tilt table and an inert-atmosphere close chamber was used to carry out both the PAW and GMAW experiments. In PAW technology, an electric arc is created between a tungsten electrode and the substrate with the help of a plasmatic gas that is carried to ionization. This gas chokes the electric arc, creating a concentrated plasma arc directed to the substrate. By means of this arc, the metallic wire that is fed thanks to the wire driver and a positioner is melted. In addition, in order to avoid the contamination of the molten material, the molten pool is protected with shielding gas. Nevertheless, in GMAW technology, the fed metallic wire is the electrode itself that, when it is touching the substrate creates an electric arc melting and depositing the material in the substrate. In this case, the molten pool must also be protected by means of shielding gas. The energy efficiency in PAW is estimated to be 50% lower than in the case of GMAW, because the metal nozzle that conducts the gas that generates the plasma acts as a very efficient heat sink [20].

The machine is equipped with a Tetric 552 AC/DC Synergic plasma welding generator and a wire feeder for PAW and a Titan XQ 400 AC puls (EWM) welding system with a M drive Rob5 XR RE(EWM) wire feeder for the GMAW welding torch. Figure 1 shows the machine and the scheme of both WAAM technologies used.

The wire material used in this investigation for each process was Invar (UTP A 8036 S). The composition of Invar, as provided by the supplier, is presented in Table 1. The diameter of the wire,  $d_{wire}$ , used as the raw material, was 1.2 mm. The substrate plate was also Invar (UTP A 8036 S) in sheet form, with a thickness of 8 mm. High purity argon (99.999%) was used as the pilot, protection

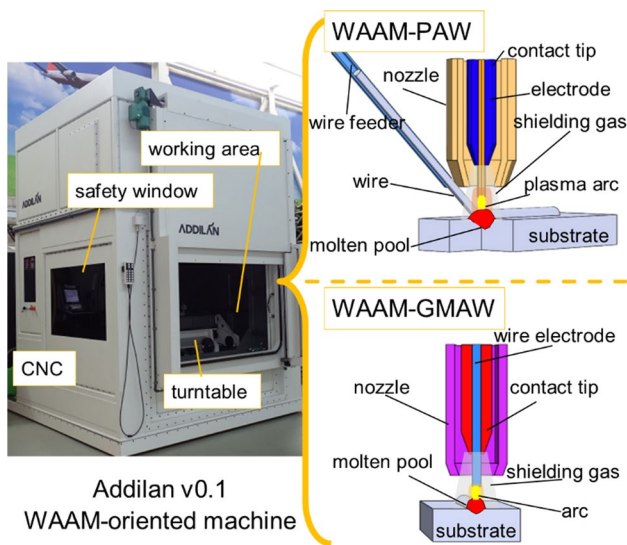


Fig. 1 Setup and WAAM technologies

Table 1 Composition of Invar wire, as provided by the supplier, by % weight

Fe	Ni	Nb	Mn	C	Cr
61.6	35.66	1.38	0.43	0.22	0.01

and plasmatic gas for PAW process and Ar (97,5%) + CO<sub>2</sub> (2,5%) as the protection gas in the case of GMAW.

The deposition sequence followed in both cases is the one shown in Fig. 2, in which both beads of the same layer are deposited in the same direction and the beads of the subsequent layer are deposited in the opposite direction in order to diminish geometrical features that occur in the beginning and end of each bead. The overlap distance in between two beads of the same layer is approximately 65% of each bead width as shown in Fig. 2.

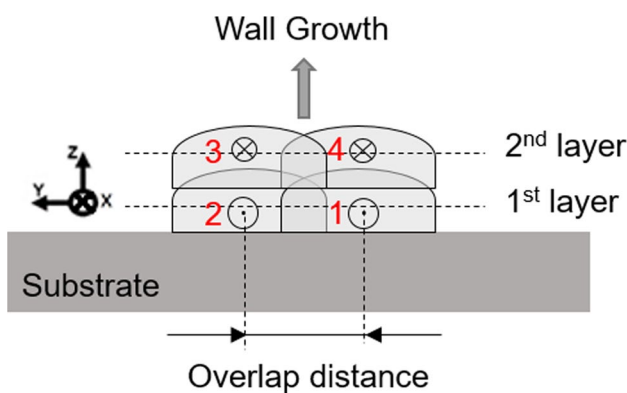


Fig. 2 Scheme of the deposition sequence in WAAM

Two 220 × 100 mm (length × height) walls have been manufactured using both WAAM technologies (PAW and GMAW). The deposition parameters in both technologies have been selected with the objective of having beads of equal geometry with good continuity and that guarantee a correct deposition in each case. A height control system is used in this study in both PAW and GMAW technologies to compensate wall height in layer-by-layer deposition. The welding parameters (current and voltage) of the process have been monitored to adapt the z-position of the nozzle.

### 2.2 Process Parameters

The purpose of the experimentation proposed in this article is to establish a comparison between two WAAM technologies: GMAW and PAW. For this purpose, their performance in manufacturing walls of the same geometry under optimum deposition conditions is compared. The correct bead geometry ratio is defined by a wetting angle, considered as the arctangent of width ( $w_{bead}$ ) and height ( $h_{bead}$ ), of 30° and a continuous bead, without the presence of spatter. To achieve a similar geometry, the deposited volume ( $V_{dep}$ ) per substrate area must be equal in both cases giving an equal bead volume per mm advanced ( $V_{bead}$ ) in both cases. The following equations illustrate the ratios, where the *Ratio* is the quotient of the wire speed ( $WFS$ ) and the travel speed ( $TS$ ), of deposition possible for this condition to be satisfied.

$$V_{bead} = A_{bead} \cdot 1mm = \frac{2}{3} \cdot w_{bead} \cdot h_{bead} \tag{1}$$

$$V_{dep} = \pi \cdot \left( \frac{d_{wire}}{2} \right)^2 \cdot Ratio \tag{2}$$

$$wetting_{angle} = arctan\left( \frac{h_{bead}}{0.5 \cdot w_{bead}} \right) \tag{3}$$

The set of parameters shown in Table 2 for each technology are the ones that provide the equal deposition ratio for achieving a proper penetration and wet angle but not introducing excessive energy to the process. The energy per unit length is higher in the case of PAW deposition as it is a less thermally efficient process. The torch heats the wire and the substrate by the action of the plasma; in the case of GMAW, the arc is produced between the wire and the substrate which results in less power required. As for the interlayer cooling stratigraphy, an interlayer cooling strategy (ICS) has been employed, similar to the one presented by Artaza et al. in [21], in which a fixed time is expected. In this case, a waiting time of 50 s was used for both technologies. The purpose of this interpass stop is to avoid the collapse of the wall as it grows in height. In addition, the energy input has been reduced by 10% from the second pass onwards.

**Table 2** Deposition conditions in the tests performed

Technology	Energy [J/mm]	TS [mm/min]	WFR [m/min]	Ratio [mm/mm]	ICS [s]
PAW	986	600	6	10	50
GMAW	446	800	8	10	50
Technology	Plasma gas flow rate [L/mm]	Nozzle diameter [mm]	Arc current [A]	Arc voltage [V]	Shielding gas flow rate [L/mm]
PAW	1.2	20	290	34	12
GMAW	-	20	220	27	17

Figure 3 shows the plan view of the beads obtained with the two technologies studied. The width and height of the bead have been measured and show comparable results. Being the PAW bead slightly wider, 2.51 compared to 2.67 for GMAW, and higher, 7.05 compared to 6.87 for GMAW, but with similar geometrical conditions, with the same ratios, the bead width depends on the melt pool width produced by the heat that is not used in the wire fusion.

The average width and height values measured on both beads have been obtained by means of a laser profilometer installed on the machine. This laser allows the reconstruction of the initial bead in the cases of GMAW (Fig. 4a) and PAW (Fig. 4b). The continuity of the bead is observed in both technologies, which agrees with a visual inspection. The bead height for GMAW is approximately 3 mm while it was found to be approximately 2.7 mm for PAW. As for the bead width determined by the profilometer, it is 6.57 mm at 1/3 of the maximum height in GMAW and 7.09 mm wide at the same Z-height position in the case of PAW.

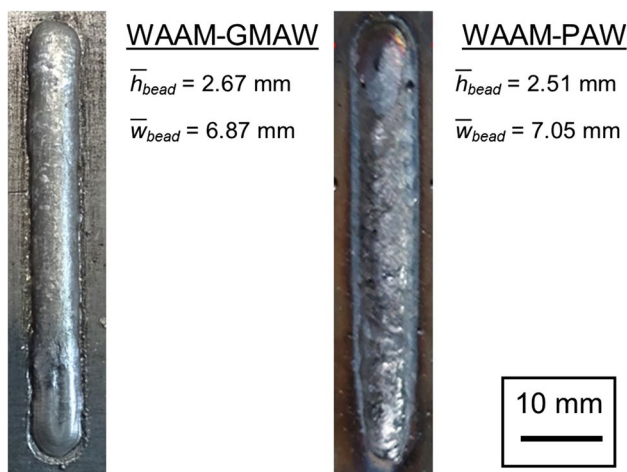
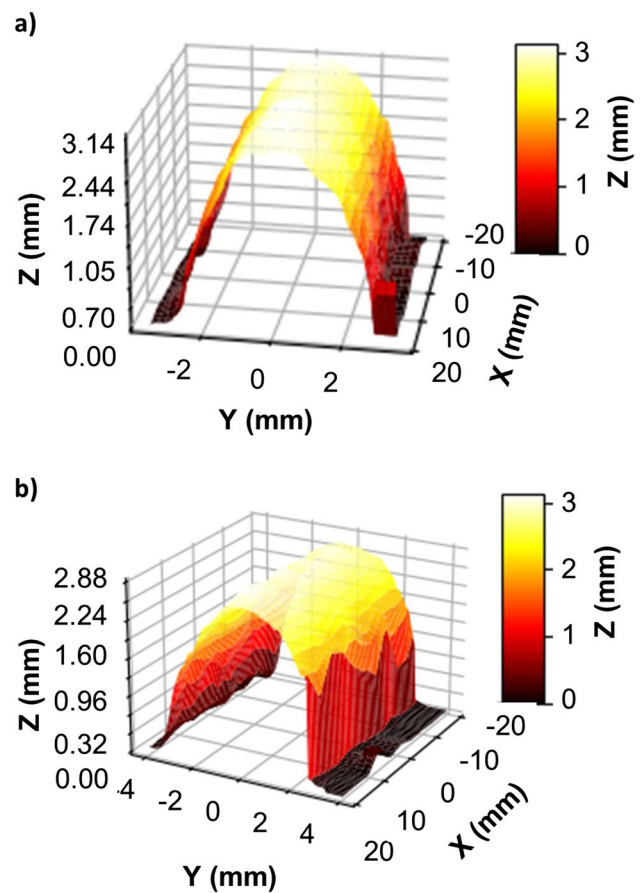
Metallographic and Mechanical Characterization.

Evaluation of mechanical properties was made by means of tensile testing and hardness values. The specimens were

obtained from the manufactured walls following the scheme shown in Fig. 5.

Specimens for tensile testing were obtained in two different directions of the wall (horizontal and vertical) following ISO 6892–1, 3 specimens were machined from each wall in the horizontal direction and the other 3 in the vertical direction. Mechanical testing was carried out at room temperature and with a speed of 1 mm/min (less than 5 MPa/s in the elastic region) using an Instron 5585H electronic machine with a contact extensometer and a load cell of 100 kN.

Both micro- and macrostructures were observed with an Eclipse MA200 (Nikon) microscope once the samples had

**Fig. 3** Bead zero obtained in WAAM-GMAW and WAAM-PAW**Fig. 4** Bead zero reconstruction in the case of **a** GMAW and **b** PAW

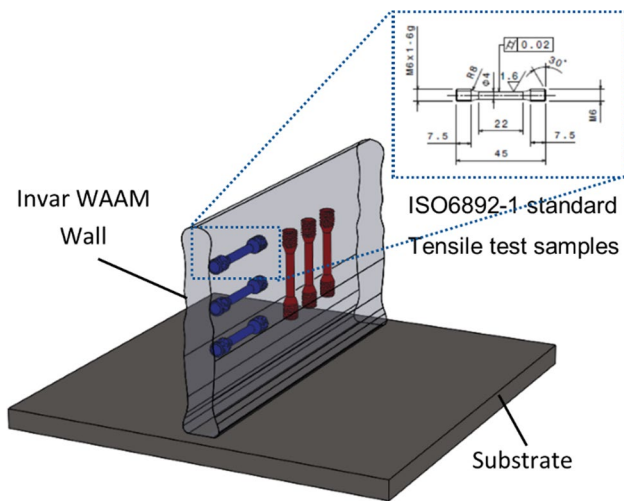
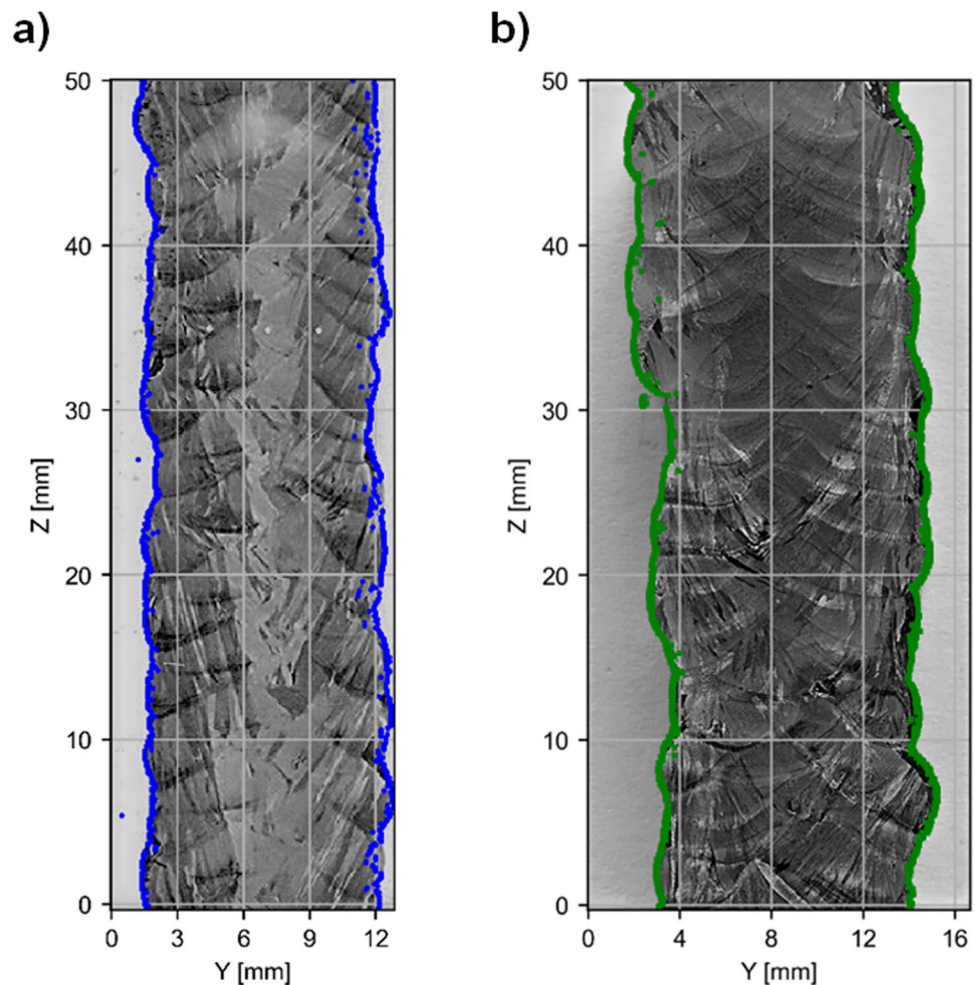


**Fig. 5** Scheme of the specimens obtained for the mechanical testing and metallographic analysis in the manufactured walls

been transversely cross-sectioned with a metallic saw from the central part of the wall at different wall heights (upper,

**Fig. 6** Edges of the wall manufactured by means of **a** GMAW and **b** PAW technology



middle, bottom). They were then polished using a series of abrasive grinding papers of decreasing coarseness from 1200 grit, followed by final diamond suspension polishing before they were etched in Kroll’s reagent. A Duramin A-300 (Struers) testing machine was employed for the Vickers hardness testing at room temperature following standard ISO 6507–1 (Normalización Española, Materiales Metálicos, UNE- EN ISO 6507–1, 2018) with a 10-kgf (98 N) load.

### 3 Results and Discussion

#### 3.1 Wall Geometry

This section analyzes the results observed in the geometry of the part. This analysis is determinant when defining the effective wall resulting from the manufacturing process of the part, as already mentioned in previous papers by these authors [14]. It is a critical factor when it comes to subsequent finishing stages through machining processes [22] since the geometry resulting from the additive stage is considered a near net shape (NNS). Figure 6 shows the

edge enhancement of the macrographic images of the walls obtained by both technologies. We have increased the sharpness and contrast of the macrographic images and analyzed in grayscale the intensity obtained by means of a threshold the points that define the edge of the wall.

By means of the distance between the wall edges obtained, the width of the wall at each height is calculated. Figure 7 shows the comparison of the wall width in both technologies and the true wall width (TWW) which is the maximum effective wall value in which a machined rectangular wall could be inscribed. In green dots the wall thickness at different heights for PAW and in blue dots for GMAW. The dashed line passes through the minimum point that defines the effective wall in both cases. The TWW value for PAW is 9.5 mm compared to 8.93 mm for GMAW.

The summary shown in Table 3 is extracted from the widths obtained along the Z-direction. The wall width values are higher in the case of using PAW technology; this is due to the deposition conditions used. Although the value of the effective wall is higher than expected, the variation of the same is also higher, which implies some inefficiency in the use of the material. This difference is not substantial so it could be established that both technologies have a similar wall geometry with a slightly better performance in the case of GMAW technology. Table 3 shows that the maximum (11.89 mm compared to 10.26 mm), mean (10.86 mm compared to 9.77 mm), and minimum (9.50 mm compared to 8.93 mm) width values of the PAW wall are higher than those of GMAW. Although the width variability of PAW expressed as standard deviation (std) is higher, almost double, than that observed in GMAW. This fact is due to the greater variability in the mechanics of drop deposition, which is more erratic in PAW technology, as it is a non-coaxial process.

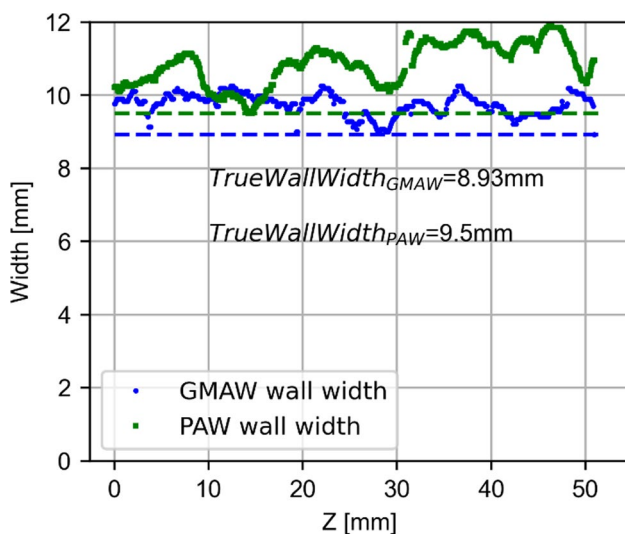


Fig. 7 True wall width (TWW) obtained on both technologies

**Table 3** Geometric characteristics of the wall manufactured in both technologies

Technology	Min	Max	Mean	Median	Std
WAAM-GMAW	8.93	10.26	9.75	9.77	0.30
WAAM-PAW	9.50	11.89	10.86	10.88	0.59

### 3.2 Microstructural Analysis

Microstructural analysis of both WAAM walls has been carried out considering the three planes of each wall. First, the microstructure of the substrate sheet in both cases has a uniform and fine equiaxed well-defined grains. After the deposition of the walls, in Fig. 8, can be seen the macrographs of the two walls. In these images, the fusion lines of subsequently deposited layers are appreciated exposing the identity of these walls manufactured layer by layer.

At the macroscopic level, either using PAW or GMAW technology, grains with a dendritic substructure are obtained. In both cases, in the central part of the walls, these grains are columnar or elongated large grains that grow in the wall growing direction (z-direction) as shown in Fig. 8. Furthermore, in the edges of the walls and in their top part, equiaxed grains can be observed. This is because after the deposition of each layer the material is cooled, and the heat dissipation is greater in these corners than in the central part. In this manner, the temperature gradient is large in the central part, which is adequate for the growth of columnar grains. The

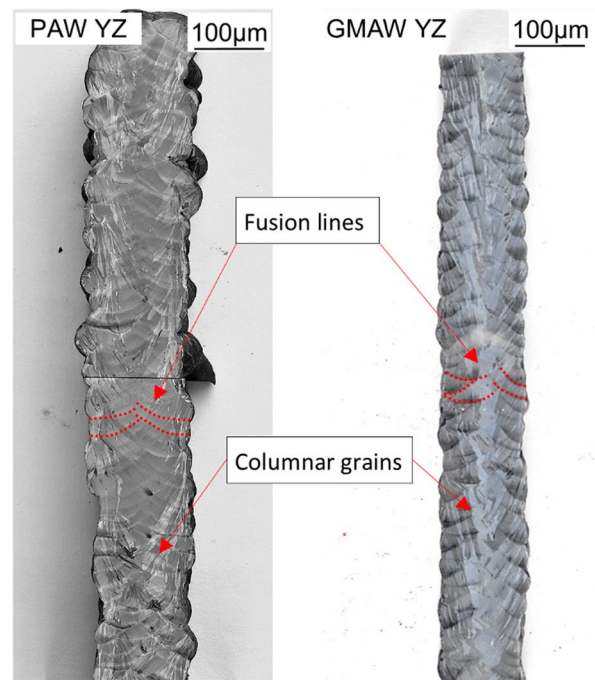


Fig. 8 YZ planes macrographs of PAW and GMAW deposited walls

columnar grains present a typical epitaxial growth morphology, and evidently, they have a perpendicular direction of the fusion lines because the grains grow preferentially in a direction of the heat dissipation.

In contrast, in the edges of the walls, this gradient is not so high, and the microstructure becomes equiaxed. This phenomenon also can be properly appreciated in XY plane of Fig. 9 where in the central part of both walls appears the columnar structure and, in the edges, the equiaxed structure. These two types of grains are similar in size with both technologies.

For more details, in the other directions of the walls (Fig. 9), similar morphologies for both technologies are observed. In the XZ plane layer height can be measured, being higher, approx. 2.5 mm in the case of GMAW compared to 2 mm in the case of PAW, probably due to the lower heat input during the deposition process. The heat input is calculated following the equation  $HI = I \cdot V / TS$ , being 446 J/mm for GMAW, half of the 986 J/mm of PAW. In the XY direction, as was mentioned above, columnar grains in the center of the walls are shown and smaller equiaxed grains in their periphery as the heat dissipation is faster on the outside of the wall which is directly in contact with the air.

At a microstructural level, as shown in Fig. 10, dendritic structures are observed in the three directions of the material after the manufacturing of the walls using both technologies. Material obtained via PAW turns out to be more anisotropic than in the case of GMAW, shown some differences in the morphology of the three different directions with combined zones of thicker and finer dendritic structures and with grains with more marked dendritic structures than others. These differences in the microstructure of the material obtained using PAW or GMAW is related to the differences in the energy applied during the process and thus, the different temperatures achieved for both technologies and the heat dissipation variation in between

them. The temperature gradient is higher in the case of PAW and therefore, anisotropy in the microstructure is caused.

As was demonstrated by Liu et al. [8], when the following bead is deposited, a part of the previous one, which is dependent on the overlap distance, is remelted. Then, a melt pool is created with the new feed material and the part of the material of the previous bead. In this way, the already deposited material suffers a heat treatment when the subsequent bead is deposited. In this study, it is found from Fig. 11 that for both walls, remelting zones are formed in the junction zone of two subsequent layers that are clearly observed in the XZ plane. Furthermore, it is concluded that both remelting regions are similar in size because both technologies work with an electric arc to deposit the material layer by layer.

Related to this, Asgari et al. [21] concluded in Invar 36 samples manufactured using PBF-LB/M technology that the dominant solidification substructure in the analyzed samples was the cellular dendrite structure. Nevertheless, near the fusion lines, they found areas with different structures (with planar morphology, cellular dendrites, columnar dendrites, or equiaxed ones) depending on the ratio between the thermal gradient and the solidification rate. In this study, as can be seen in Fig. 11 (1 and 3 parts), in both technologies, in the remelting region and the area above its, coarse dendrites are observed. The reason behind this is that this material was reheated during the deposition of the following bead when it had not yet cooled down completely, reducing the cooling rate and obtaining a coarser grain size. However, in the area behind the remelted region, a finest dendritic structure can be observed (2 and 4 parts).

Consecutively, the main observed features in Invar36 are similar both for PAW- and GMAW-based WAAM manufacturing, with a resulting isotropic material in the case of GMAW and a more anisotropic material in the case of PAW.

**Fig. 9** XZ and XY planes of PAW and GMAW deposited material

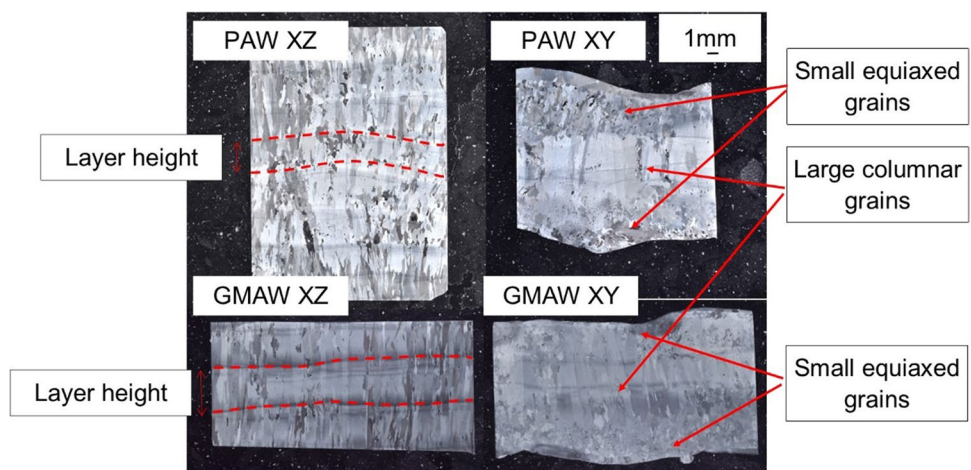
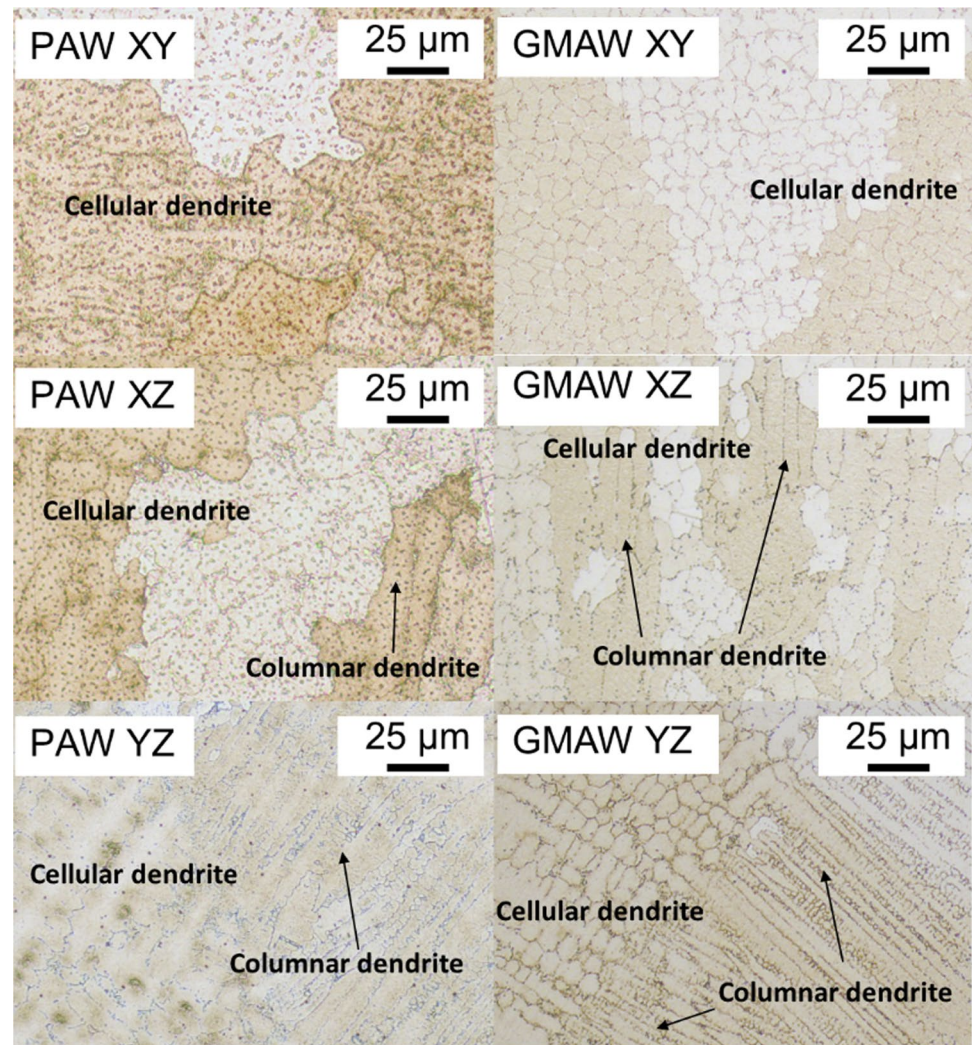


**Fig. 10** Microstructure of the three planes of each wall at  $\times 400$



### 3.3 Mechanical Properties

In this section, the mechanical properties measured on the wall obtained by both technologies are analyzed. The analysis will focus on the analysis of the hardness at different wall heights and the mechanical properties derived from tensile tests. Hardness values have been obtained in both specimens built using PAW and GMAW at three different heights of the walls as shown in Fig. 12. A slight increase in hardness values is observed in the middle part of the walls manufactured by PAW, being appreciably that also variability increases. The presence of precipitates derived from the thermal cycles to which the material is subjected in this type of technology causes the hardness results to increase locally. The hardness values are not higher than those observed in the material obtained by the conventional method [23].

Figure 13 shows the stress–strain curve of each of the tested specimens of the wall manufactured by PAW (a) and by GMAW (b). Higher yield strength (YS) and ultimate

tensile strength (UTS) results are observed in the cases of the specimens in the horizontal direction due to the anisotropy of the materials manufactured with WAAM technology in which the directionality of the dendritic formations that define the microstructure. The difference in behaviour is more evident in the case of PAW, where in the horizontal direction there is a greater strength (486 MPa) and in the vertical direction a more ductile behaviour where the strength is lower (463 MPa) but the elongation at break is higher (51% compared with 29% in the horizontal direction). Finally, the UTS and YS results are slightly higher for GMAW than for PAW, the mean value of the UTS in the case of GMAW is 485 MPa 10 MPa more than in the case of PAW, suggesting that a lower thermal input improves the strength.

In the following Table 4, the numerical summary of the measured values of the stress–strain curves are shown. From the results shown in the table, a slightly lower value for UTS compared to the standard is induced, while the values for elongation and YS meet or even exceed those described in



**Fig. 11** Remelting zone in between layers of both GMAW and PAW walls

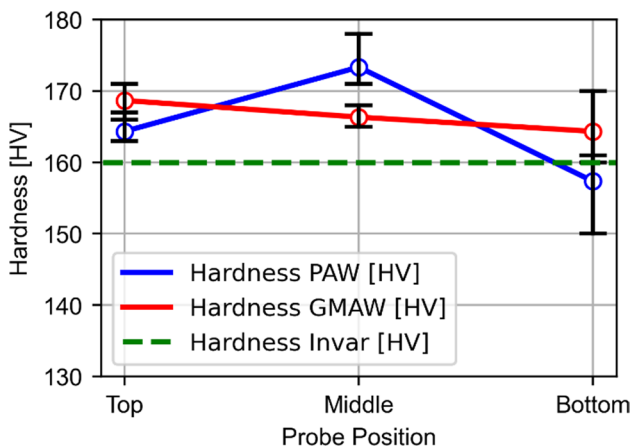
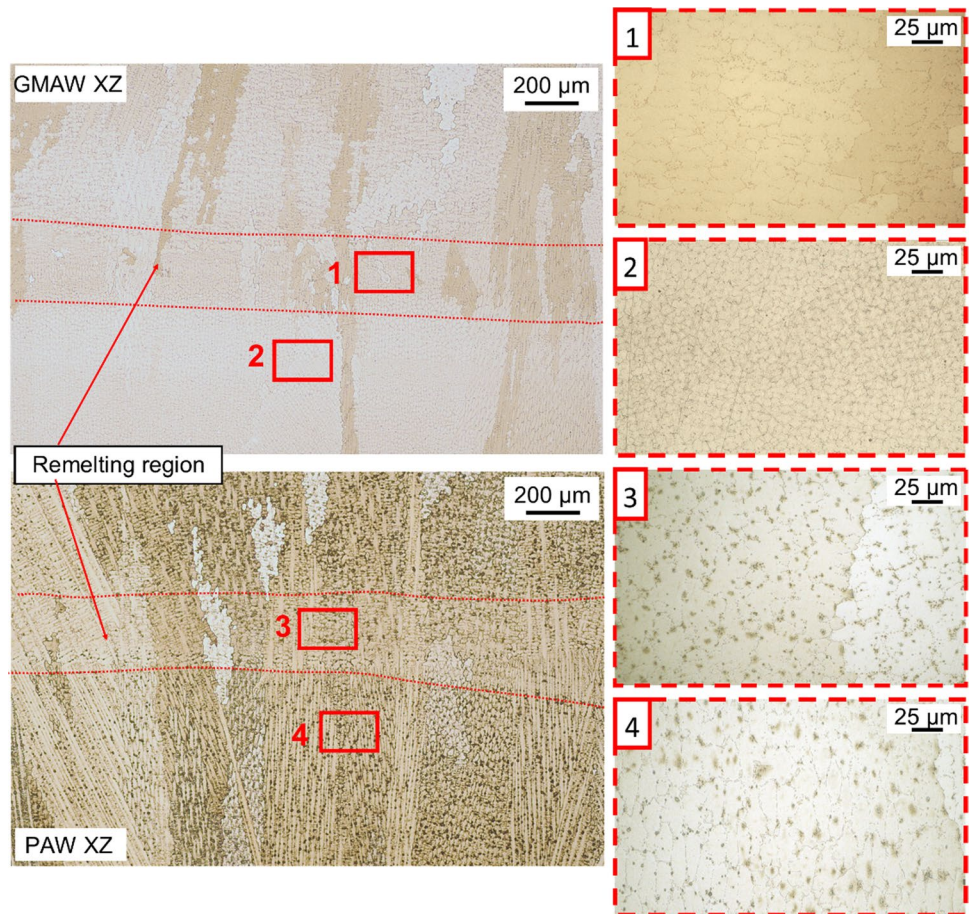


**Fig. 12** Hardness values in the Invar walls built using PAW and GMAW

the standard. The lowest observed value for UTS is 455 MPa in a vertical direction test in PAW technology; in the same test, YS is also the lowest with 263 MPa. Finally, the worst elongation at break occurs in the case of PAW technology but this time in the horizontal direction with a value of 27%. This leads to the conclusion that the PAW technology is

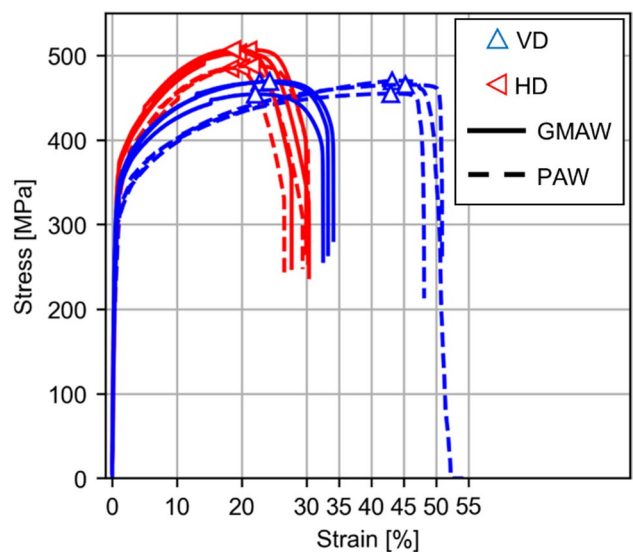


**Fig. 13** Results of tensile tests of the wall manufactured by **a** PAW and **b** GMAW

more disadvantageous since in this scenario, given the anisotropy of the results, the worst values of mechanical properties are observed.

**Table 4** Deposition conditions in the tests performed

Material (technology)	Sample direction	Yield strength (YS) (MPa)	Ultimate tensile strength (UTS) (MPa)	Elongation (%)
Invar PAW	Horizontal	277 ± 5	486 ± 1	29 ± 2
	Vertical	270 ± 7	464 ± 7	49 ± 2
Invar GMAW	Horizontal	345 ± 5	505 ± 2	29 ± 1
	Vertical	305 ± 6	464 ± 9	33 ± 1
Invar conventional [23]		276	518	34

Anisotropy observed in PAW during the analysis of the microstructure is also observed in the mechanical properties. While the results obtained for the GMAW process are very similar in both directions, there is a remarkable difference in the results obtained for vertical and horizontal directions of the PAW technology, being more ductile in the vertical direction.

## 4 Conclusions

The fabrication of two Invar walls using PAW and GMAW has been detailed, as well as the characterization carried out in terms of metallography and mechanical properties of the material. The main conclusions are presented as follows:

- Both technologies produce similar geometries (width and true wall width), being more variable in the case of PAW and thus, indicating to be a less efficient process compared to GMAW.
- At a macrostructural level, no remarkable differences are observed between technologies. Columnar grains are observed in the center of the wall with smaller ones in the periphery, with marked fusion lines in between layers.
- Main microstructural features have been detected in both GMAW and PAW walls (columnar and cellular dendrites), with dendritic grains in all three planes. More diffused dendritic structures are observed in the case of PAW with thicker structures compared to GMAW.
- Anisotropy is observed in the microstructure of PAW technology obtained material, with thicker and finer dendrite structures and dendritic zones more marked than others.
- A slightly lower value for UTS (mean value of 485 MPa in GMAW and 475 MPa in PAW) compared to the standard (518 MPa) is induced, while the values for elongation and YS meet or even exceed those described in the standard.
- While the results of elongation obtained for the GMAW process are very similar in both directions, mean elongation at break in vertical direction is 33% and 29% in horizontal direction, there is a remarkable difference in the results obtained for vertical and horizontal directions

of the PAW technology, being more ductile in the vertical direction, 51% in comparison with 29% in the horizontal direction.

**Funding** Open Access funding provided by Universidad Pública de Navarra. The authors acknowledge funding from the Basque Government to the HARITIVE project [ZE-2017/00038], HARIPLUS project [ZE-2019/00352], QUALYFAM project [kk-2020/00042], and the European Institute of Innovation and Technology to DEDALUS project [reference ID 20094].

## Declarations

**Conflict of Interest** The authors declare no competing interests.

**Open Access** This article is licensed under a Creative Commons Attribution 4.0 International License, which permits use, sharing, adaptation, distribution and reproduction in any medium or format, as long as you give appropriate credit to the original author(s) and the source, provide a link to the Creative Commons licence, and indicate if changes were made. The images or other third party material in this article are included in the article's Creative Commons licence, unless indicated otherwise in a credit line to the material. If material is not included in the article's Creative Commons licence and your intended use is not permitted by statutory regulation or exceeds the permitted use, you will need to obtain permission directly from the copyright holder. To view a copy of this licence, visit <http://creativecommons.org/licenses/by/4.0/>.

## References

1. Sahoo A, Medicherla VRR (2020) Fe-Ni Invar alloys: a review. *Mater Today Proc* 43:2242–2244. <https://doi.org/10.1016/j.matpr.2020.12.527>
2. Khanna N, Gandhi A, Nakum B, Srivastava A (2018) Optimization and analysis of surface roughness for INVAR-36 in end milling operations. *Mater Today Proc* 5:5281–5288. <https://doi.org/10.1016/j.matpr.2017.12.111>
3. Cooke S, Ahmadi K, Willerth S, Herring R (2020) Metal additive manufacturing: Technology, metallurgy and modelling. *J Manuf Process* 57:978–1003. <https://doi.org/10.1016/j.jmapro.2020.07.025>
4. Yakout M, Elbestawi MA, Veldhuis SC (2019) Density and mechanical properties in selective laser melting of Invar 36 and

- stainless steel 316L. *J Mater Process Technol* 266:397–420. <https://doi.org/10.1016/j.jmatprotec.2018.11.006>
5. Wei K, Yang Q, Ling B, Yang X, Xie H, Qu Z, Fang D (2020) Mechanical properties of Invar 36 alloy additively manufactured by selective laser melting. *Mater Sci Eng, A* 772:138799. <https://doi.org/10.1016/j.msea.2019.138799>
  6. Yang Q, Wei K, Yang X, Xie H, Qu Z, Fang D (2020) Microstructures and unique low thermal expansion of Invar 36 alloy fabricated by selective laser melting. *Mater Charact* 166:110409. <https://doi.org/10.1016/j.matchar.2020.110409>
  7. Qiu C, Adkins NJE, Attallah MM (2016) Selective laser melting of Invar 36: Microstructure and properties. *Acta Mater* 103:382–395. <https://doi.org/10.1016/j.actamat.2015.10.020>
  8. Liu T, Gao Z, Ling W, Wang Y, Wang X, Zhan X, Liu D, Lei Y, Martin P (2021) Effect of heat accumulation on the microstructure of Invar alloy manufactured by multi-layer multi-pass laser melting deposition. *Opt Laser Technol* 144:107407. <https://doi.org/10.1016/j.optlastec.2021.107407>
  9. Zhan X, Qi C, Zhou J, Liu LJ, Gu D (2019) Effect of heat input on the subgrains of laser melting deposited Invar alloy. *Opt Laser Technol* 109:577–583. <https://doi.org/10.1016/j.optlastec.2018.08.013>
  10. Li H, Chen B, Tan C, Song X, Feng J (2020) Microstructure evolution and mechanical properties of laser metal deposition of Invar 36 alloy. *Opt Laser Technol* 125:106037. <https://doi.org/10.1016/j.optlastec.2019.106037>
  11. Bobbio LD, Otis RA, Borgonia JP, Dillon RP, Shapiro AA, Liu ZK, Beese AM (2017) Additive manufacturing of a functionally graded material from Ti-6Al-4V to Invar: Experimental characterization and thermodynamic calculations. *Acta Mater* 127:133–142. <https://doi.org/10.1016/j.actamat.2016.12.070>
  12. Bocklund B, Bobbio LD, Otis RA, Beese AM, Liu ZK (2020) Experimental validation of Scheil–Gulliver simulations for gradient path planning in additively manufactured functionally graded materials. *Materialia*. 11. <https://doi.org/10.1016/j.mtla.2020.100689>.
  13. Jin W, Zhang C, Jin S, Tian Y, Wellmann D, Liu W (2020) Wire arc additive manufacturing of stainless steels: a review. *Appl Sci* 10:1563. <https://doi.org/10.3390/app10051563>
  14. Aldalur E, Veiga F, Suárez A, Bilbao J, Lamikiz A (2020) Analysis of the wall geometry with different strategies for high deposition wire arc additive manufacturing of mild steel. *Metals* 10:1–19. <https://doi.org/10.3390/met10070892>
  15. Fowler J, Nycz A, Noakes M, Masuo C, Vaughan D (2019) Wire-arc additive manufacturing: Invar deposition characterization, Solid Freeform Fabrication 2019: Proceedings of the 30th Annual International Solid Freeform Fabrication Symposium - An Additive Manufacturing Conference, SFF 2019. 616–624
  16. Chu J (2020) Investigating the feasibility and impact of integrating wire-arc additive manufacturing in Aerospace Tooling Applications. PhD. MIT Department of Mechanical Engineering
  17. Veiga F, Suarez A, Aldalur E, Artaza T (2022) Wire arc additive manufacturing of Invar parts: bead geometry and melt pool monitoring. *Measurement* 189:110452. <https://doi.org/10.1016/j.measurement.2021.110452>
  18. Leicher M, Kamper S, Treutler K, Wesling V (2020) Multi-material design in additive manufacturing — feasibility validation. *Weld World* 64:1341–1347
  19. Treutler K, Kamper S, Leicher M, Bick T, Wesling V (2019) Multi-material design in welding arc additive manufacturing. *Metals*. 9. <https://doi.org/10.3390/met9070809>
  20. Evans DM, Huang D, McClure JC, Nunes AC (1998) Arc efficiency of plasma arc welding. *Weld J* 77(2):53–58
  21. Asgari H, Salarian M, Ma H, Olubamiji A, Vlasea M (2018) On thermal expansion behavior of invar alloy fabricated by modulated laser powder bed fusion. *Mater Des* 160:895–905. <https://doi.org/10.1016/j.matdes.2018.10.025>
  22. Chen C, Ma B, Liu B, He J, Xue H, Zuo Y, Li X (2019) Refinement mechanism and physical properties of arc melted invar alloy with different modifiers. *Mater Chem Phys* 227:138–147
  23. ASTM B753–07(2018), Standard specification for thermostat component alloys, ASTM International, West Conshohocken, PA, 2018, [www.astm.org](http://www.astm.org). Accessed 24 Sept 2021

**Publisher's Note** Springer Nature remains neutral with regard to jurisdictional claims in published maps and institutional affiliations.